ACS APPLIED MATERIALS & INTERFACES

www.acsami.org

Research Article

Insight into Ion Diffusion Dynamics/Mechanisms and Electronic Structure of Highly Conductive Sodium-Rich $Na_{3+x}La_xZr_{2-x}Si_2PO_{12}$ ($0 \leq x \leq 0.5$) Solid-State Electrolytes

Fei Sun,[¶] Yuxuan Xiang,[¶] Qian Sun, Guiming Zhong, Mohammad Norouzi Banis, Weihan Li, Yulong Liu, Jing Luo, Ruying Li, Riqiang Fu, Tsun-Kong Sham,* Yong Yang,* Xuhui Sun,* and Xueliang Sun*

Cite This: *ACS Appl. Mater. Interfaces* 2021, 13, 13132−13138

Read Online

ACCESS | Metrics & More | Article Recommendations | Supporting Information

ABSTRACT: Solid-state electrolytes (SSEs) have attracted considerable attention as an alternative for liquid electrolytes to improve safety and durability. Sodium Super Ionic CONductor (NASICON)-type SSEs, typically $Na_3Zr_2Si_2PO_{12}$, have shown great promise because of their high ionic conductivity and low thermal expansivity. Doping La into the NASICON structure can further elevate the ionic conductivity by an order of magnitude to several mS/cm. However, the underlying mechanism of ionic transportation enhancement has not yet been fully disclosed. Herein, we fabricate a series of $Na_{3+x}La_xZr_{2-x}Si_2PO_{12}$ ($0 \leq x \leq 0.5$) SSEs. The electronic and local structures of constituent elements are studied via synchrotron-based X-ray absorption spectroscopy, and the ionic dynamics and Na-ion conduction mechanism are investigated by solid-state nuclear magnetic resonance spectroscopy. The results prove that La^{3+} ions exist in the form of phosphate impurities such as $Na_3La(PO_4)_2$ instead of occupying the Zr^{4+} site. As a result, the increased Si/P ratio in the NASICON phase, accompanied by an increase in the sodium ion occupancy, makes a major contribution to the enhancement of ionic conductivity. The spin−lattice relaxation time study confirms the accelerated Na^+ motions in the altered NASICON phase. Modifications on the Si/P composition can be a promising strategy to enhance the ionic conductivity of NASICON.

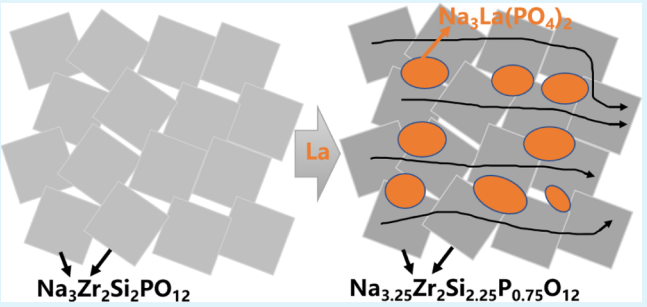

KEYWORDS: *NASICON, solid-state electrolyte, NMR, XAS, La doping, high ionic conductivity, diffusion mechanism*

1. INTRODUCTION

Rechargeable batteries are regarded as the most promising energy storage technology because of their reliability and high energy conversion efficiency. Although Li-ion batteries (LIBs) have been widely used in portable electronic devices, Na-ion batteries (NIBs) are considered as the most potential candidate to replace LIBs because of their nontoxicity, low cost, and elemental abundance.[1−6] Solid-state electrolytes (SSEs) are an ultimate component for NIBs because conventional liquid electrolytes (LEs) still inherit concerns of flammability and potential leakage. SSEs are expected to improve the durability and safety as well as simplify the cell design for future NIBs. Eventually, all-solid-state NIBs using high-voltage cathodes and Na metal anodes are projected to achieve even higher energy densities than LE-based NIBs.[7,8]

Among the Na-ion conducting SSEs, sodium Super Ionic CONductor (NASICON) with a general formula of $Na_{1+n}Zr_2Si_nP_{3-n}O_{12}$ ($1.6 \leq n \leq 2.4$) has attracted the most attention because of its high ionic conductivity and low thermal expansivity.[9−16] The NASICON structure, first reported by Hong,[17] generally consists of a rigid three-dimensional network of ZrO_6 octahedral and PO_4^{3-}/SiO_4^{4-} tetrahedral sharing corners. The interconnected channels in this framework provide efficient conduction pathways for Na^+ ions (Figure 1a). Although the original form of $Na_3Zr_2Si_2PO_{12}$ already exhibits a high ionic conductivity of 10^{-4} S/cm at room temperature, over the past decades, constant efforts have been dedicated to further improve its ionic conductivity for feasible electrochemical performance.[8−13,16] A common approach to modify the NASICON is so-called element substitution with heteroatoms such as Zn, Sc, Ce, Zr, La, and so forth. La is one of the most effective substitution elements reported for NASICON that pushes the ionic conductivity to the order of 10^{-3} S/cm.[8] However, the dynamics and ionic conducting

Received: December 9, 2020
Accepted: February 19, 2021
Published: March 15, 2021

https://dx.doi.org/10.1021/acsami.0c21882
ACS Appl. Mater. Interfaces 2021, 13, 13132−13138

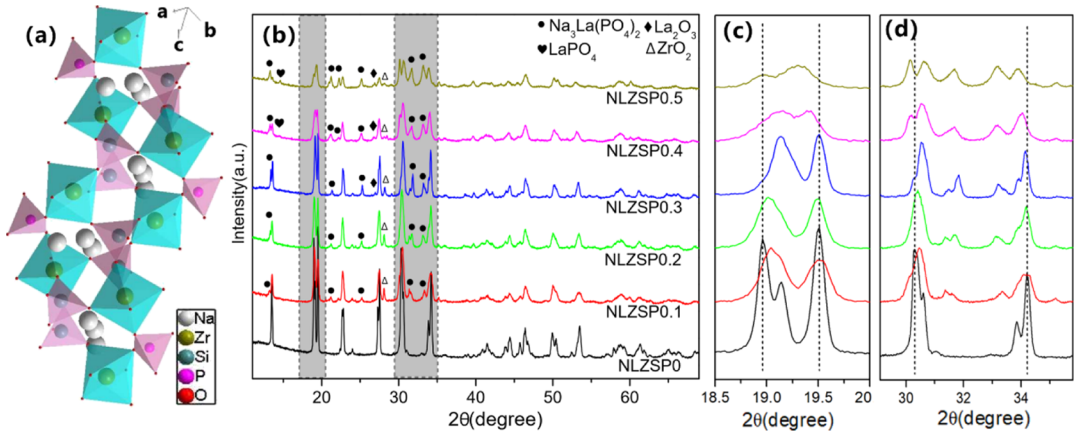

Figure 1. (a) Schematic of a general NASICON structure. (b) XRD patterns of NLZSPx (x = 0, 0.1, 0.2, 0.3, 0.4, and 0.5); (c,d) are magnified views of the selected regions.

mechanism of NASICON $Na_{3+x}La_xZr_{2-x}Si_2PO_{12}$ ($0 \le x \le 0.5$) are not yet clear.

In order to understand the mechanism of the ionic conductivity enhancement by La doping in NASICON, we use synchrotron-based soft X-ray absorption spectroscopy (XAS) to study the electronic and local structure of P and Si elements and solid-state nuclear magnetic resonance (SS-NMR) relaxometry to investigate the Na^+ transport in the La-doped NASICON. A series of $Na_{3+x}La_xZr_{2-x}Si_2PO_{12}$ (denoted as NLZSPx, where $0 \le x \le 0.5$) are prepared to disclose the effects of La doping concentration. We find that the performance of La-doped NASICON SSEs is highly correlated with the diffusion parameters such as activation barriers for single-ion jumps and hopping rates of Na^+ ions. The understanding on the ionic conducting mechanism and Na^+ migration in La-doped NASICON can be of great guiding significance for further improving the ionic conductivity in similar electrolytes.

2. EXPERIMENTAL SECTION

2.1. Material Synthesis. Nominal composition La-doped NASICON NLZSPx (x = 0, 0.1, 0.2, 0.3, 0.4, and 0.5) SSEs were synthesized by a sol−gel method. $NaNO_3$ (≥99.0%, Sigma-Aldrich), $La(NO_3)_3{\cdot}6H_2O$ (≥99.99%, Sigma-Aldrich), $NH_4H_2PO_4$ (≥98%, Sigma-Aldrich), $Si(OC_2H_5)_4$ (tetraethyl orthosilicate, ≥98%, Sigma-Aldrich), and $C_{12}H_{28}O_4ZR$ [zirconium(IV) propoxide solution, 70 wt % in 1-propanol, Sigma-Aldrich] were used as the starting materials with citric acid as a chelating agent. First, a mixture of tetraethyl orthosilicate, zirconium(IV) propoxide solution, citric acid, ethanol, and H_2O was stirred at 60 °C overnight. Second, $La(NO_3)_3{\cdot}6H_2O$, 10% excessive $NaNO_3$, and 10% excessive $NH_4H_2PO_4$ were dissolved in deionized water and then added to the previous solution. The collosol was heated at 70 °C and stirred until a dried gel was obtained, which required several hours. Then, the obtained dry xerogel was first calcined in air at 500 °C for 2 h and then 1050 °C for 10 h. The calcined powder was ground and pressed into pellets (diameter 13 mm, thickness 1 mm) and sintered at 1250 °C for 12 h. White ceramic pellets with a diameter between 11.2 and 11.5 mm and a thickness of around 0.9 mm can be obtained after sintering. The pellets obviously shrunk compared to those before sintering. $Na_3La(PO_4)_2$ was synthesized by heating the mixture of $NaNO_3$ and $La(NO_3)_3{\cdot}6H_2O$ at 700 °C for 12 h.

2.2. Material Characterization. The crystal structure and phase composition of the NLZSPx (x = 0, 0.1, 0.2, 0.3, 0.4, 0.5) SSEs were characterized via X-ray diffraction (XRD) using a D8 ADVANCE (Bruker Co.) diffractometer with Cu Kα X-ray source in the range of 10−70° with a step of 0.01° per seconds. Scanning electron microscopy (SEM) images and energy-dispersive spectroscopy (EDS) mappings were collected using a Hitachi 4800 scanning electron microscope equipped with an EDS detector. The working voltage for the EDS mapping was 20 kV.

2.3. Electrochemical Measurements. The ionic conductivity of NLZSPx (x = 0, 0.1, 0.2, 0.3, 0.4, 0.5) SSEs was measured by electrochemical impedance spectroscopy (EIS). Nyquist plots were recorded by a Gamry electrochemical system in the frequency range between 100 mHz and 100 kHz with an AC voltage of 5 mV. Au electrodes were coated on the NLZSPx pellets by sputtering before the conductivity measurement.

2.4. XAS Measurements. XAS measurements at the fluorescence yield modes of P K-edge and Si K-edge were performed on the soft X-ray micro characterization beamline (SXRMB) end station at the Canadian Light Source with powder samples. SXRMB was equipped with a double-crystal monochromator with two sets of interchangeable crystals, InSb(111) and Si(111), and the operating energy range was from 1.7 to 10 keV. All XAS spectra were normalized to the incident photon flux and calibrated with standard compounds.

2.5. NMR Experiments. ^{23}Na spin−lattice relaxation time (T_1) measurements as well as ^{29}Si and ^{31}P magic angle spinning (MAS) NMR spectra were acquired on a Bruker AVANCE III 400 MHz spectrometer at Larmor frequencies of 105.9, 79.5, and 162.0 MHz, respectively. The chemical shifts of ^{23}Na, ^{29}Si, and ^{31}P were calibrated using 1 M NaCl (0 ppm), trimethylsilyl propanoic acid (0 ppm), and ammonium dihydrogen phosphate (1 ppm), respectively. A 4 mm Bruker MAS probe was employed for the measurements at a spinning rate of 12 kHz. ^{23}Na T_1 values were determined by using inversion recovery experiments. The ^{29}Si and ^{31}P NMR spectra were recorded using a single pulse with $\pi/4$ pulse lengths of 3 and 4.8 us and repetition times of 120 and 150 s, respectively. ^{23}Na MAS NMR spectra were also acquired on an ultrawide bore 900 MHz NMR spectrometer at the National High Magnetic Field Lab using a home-made transmission line 3.2 mm MAS probe at a spinning rate of 10 kHz.

3. RESULTS AND DISCUSSION

3.1. Crystal Structure and Microstructure of the Ceramic Electrolytes. A series of NLZSPx ($0 \le x \le 0.5$) SSEs were synthesized by a sol−gel method. The NLZSPx pellets were sintered at 1250 °C and polished before use. Figure 1b shows the XRD patterns of the NLZSPx SSEs. A major crystalline NASICON phase, a minor crystalline $Na_3La(PO_4)_2$ impurity phase and weak diffractions from La_2O_3 and $LaPO_4$ impurity phases were observed. Overall, with increasing La content, the peaks ascribed to $Na_3La(PO_4)_2$ became more intense relative to the NASICON peaks, indicating the increasing contents of the impurity phases.

https://dx.doi.org/10.1021/acsami.0c21882
ACS Appl. Mater. Interfaces 2021, 13, 13132−13138

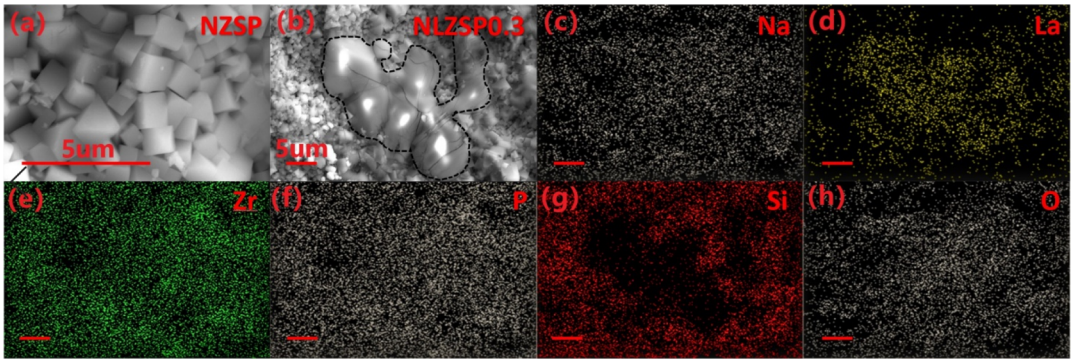

Figure 2. SEM images of (a) NLZSP0 and (b) NLZSP0.3. Corresponding EDS mappings of (c) Na, (d) La, (e) Zr, (f) P, (g) Si, and (h) O elements. The dashed line in (b) traces the boundary between the NASICON and $Na_3La(PO_4)_2$.

The formation of the $Na_3La(PO_4)_2$ phase took over part of the La^{3+} ions that were supposed to substitute the Zr^{4+} sites in the NASICON structure, meanwhile extracting some P component from the NASICON phase.[8] Figure 1c,d carefully compares the XRD patterns in the selected regions. The XRD peaks at 19.1 and 30.5° for the undoped NLZSP0 slightly shifted to higher angles as upon La doping, while the XRD peaks at 19.5 and 34.2° shifted to lower angles along with the increasing La content. Two XRD peaks at around 19° became one peak, and the peak at 30.5° split into two peaks. These observations indicated that the crystalline structure of the NLZSP*x* samples gradually changed from the monoclinic to rhombohedra structure as a result of the removal of P from the NASICON main phase to the phosphate impurity phases.[10,18] Zhang et al. reported that the lattice parameters *a* and *b* of the monoclinic structure increased while *c* decreased with La^{3+} substitution.[8] In addition, for NLZSP*x* with a high La doping content, an additional weak peak (2θ = 28.1) related to monoclinic ZrO_2 appeared. The formation of ZrO_2 impurity is common in the synthesis of NASICON-structured SSEs and difficult to avoid.[18−24] Based on previous studies, the effect of a small amount of ZrO_2 is negligible. The effects and roles of phosphate impurity phases will be discussed in later sections.

The microstructures of NLZSP0 and NLZSP0.3 were observed by SEM. The NLZSP0 SSE showed a typical NASICON feature as cubic particles with sides approximately 1−2 μm (Figure 2a). In comparison, as shown in Figure 2b, two distinct phases with different morphologies were observed in the NLZSP0.3 sample, where the $Na_3La(PO_4)_2$ impurity phase was buried in the middle of the La-doped NASICON cubes. The EDS mappings of NLZSP0.3 confirmed the distribution of the two phases (Figure 2c−h). While both the NASICON phase and the $Na_3La(PO_4)_2$ impurity phase shared common elements of Na, La, P, and O, the Si element which was primarily present in the NASICON phase could clearly depict the distributions of the two phases. The irregularly shaped phase in the middle was confirmed as the impurity phase by the absence of the Si signal. The intense La signals from the impurity region supported the claim that La^{3+} ions participated in the formation of phosphate impurity phases rather than replacing Zr^{4+} in the NASICON structure, which is consistent with the XRD results above.

Moreover, based on the fact that the formation of the $Na_3La(PO_4)_2$ impurity phase extracted some P components from the NASICON phase, the atomic ratios between Si and P elements in the resulted NASICON phase of the NLZSP*x* samples must be different from that of the original NLZSP0. For verification, Si/P atomic ratios for NLZSP0 and NLZSP0.3 were calculated based on EDS analysis on the respective NASICON phases (Figure S1). The Si/P ratio in the NASICON phase increased from the original 2:1 to around 3:1 for NLZSP0.3, confirming the loss of P component upon La doping.

3.2. Ionic Conductivity of NLZSP*x* SSEs. The ionic conductivities of the undoped NLZSP0 and the La-doped NLZSP*x* (x = 0.1, 0.2, 0.3, 0.4, and 0.5) were measured by EIS. Au thin films were deposited on both sides of the SSE pellets by sputtering as the blocking electrodes. Figure 3a compares

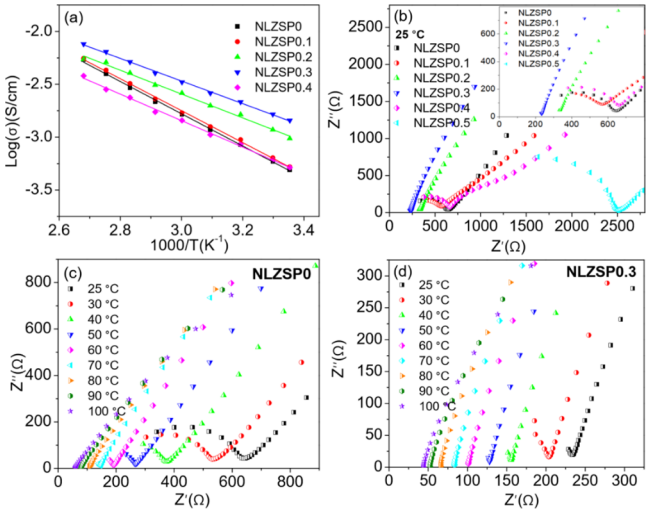

Figure 3. Temperature-dependent ionic conductivities for the different NLZSP*x* (x = 0, 0.1, 0.2, 0.3, and 0.4) SSEs over the temperature range from 25 to 100 °C. (a) Arrhenius plots of nominal composition NLZSP*x* (x = 0, 0.1, 0.2, 0.3, and 0.4) between 25 and 100 °C. (b) Impedance spectra of NLZSP*x* (x = 0, 0.1, 0.2, 0.3, 0.4, and 0.5) at 25 °C; the inset is a magnified view of the low-impedance region. Impedance spectra of (c) NLZSP0 and (d) NLZSP0.3 at different temperatures.

the temperature-dependent ionic conductivities of the NLZSP0 and NLZSP*x* SSEs from 25 to 100 °C. All SSEs exhibited Arrhenius behaviors over the temperature range, based on the good linear fit between the logarithmic ionic conductivities and the reciprocal of temperatures. Generally, a higher La doping content led to a higher overall ionic conductivity until beyond NLZSP0.3. As shown in Figure 3b, the NLZSP0.3 SSE demonstrated the smallest impedance and thus optimal ionic conductivity among the NLZSP*x* SSEs at 25

https://dx.doi.org/10.1021/acsami.0c21882
ACS Appl. Mater. Interfaces 2021, 13, 13132−13138

°C. NLZSP0.3 possessed a room-temperature ionic conductivity (1.34×10^{-3} S/cm) almost 3 times higher than that of the undoped NLZSP0 (4.89×10^{-4} S/cm), where the ionic conductivity of NLZSP0 at 25 °C was comparable with the reported values.[8−13,16] The impedance spectra for NLZSP0 and NLZSP0.3 over the full temperature range are shown in Figure 3c,d.

3.3. XAS Analysis of NLZSP*x* SSEs. P K-edge and Si K-edge X-ray absorption near-edge structure (XANES) analyses were performed for different La-doped NLZSP*x* SSEs to understand the chemical environment electronic states of P and Si elements in the different resulted NASICON phases (Figure 4). No such information was available prior to this work. The K-edge XANES originates from transitions of the 1s core level of an absorbing element to excited vacant states of proper symmetry involving the element valence orbitals. XANES provides information on the oxidation state and local symmetry. The XANES of a series of standard phosphate compounds has been recorded, and they show characteristic features in the main peak (white line) position as well as in the number and position of pre-edge and postedge peaks that can be used to identify phosphate species in the XANES spectra.[25] Figure 4a shows the normalized P K-edge XANES spectra of the La-doped NLZSP0.1, NLZSP0.3, and NLZSP0.5 SSEs together with the reference spectra of the undoped NLZSP0 and impurity $Na_3La(PO_4)_2$ for comparison. The white line energy occurred near 2153.2 eV in all P K-edge XANES, which can be assigned to a transition of the P 1s electron into an unoccupied valence electronic state formed by the overlap of P sp^3 hybrid- and O 2p-orbitals because the PO_4^{3-} group has a T_d-symmetry. A broader peak occurring at around 2169 eV is due to oxygen multiple scattering of the tetrahedral first shell nearest neighboring oxygen in the PO_4^{3-} group.[26−29] It can be seen that when *x* increased, it was accompanied by a left shift of the white line peak position, and both the white line peak and the pre-edge around 2150 eV slightly decreased gradually, which was due to structural change of the NASICON phase, such as parameter, ligand field, centrosymmetry, or spin states. These changes indicated a small distortion as the initially perfect sp^3 became distorted. In addition, the characteristic peak of impurity $Na_3La(PO_4)_2$ started to appear and became stronger gradually.

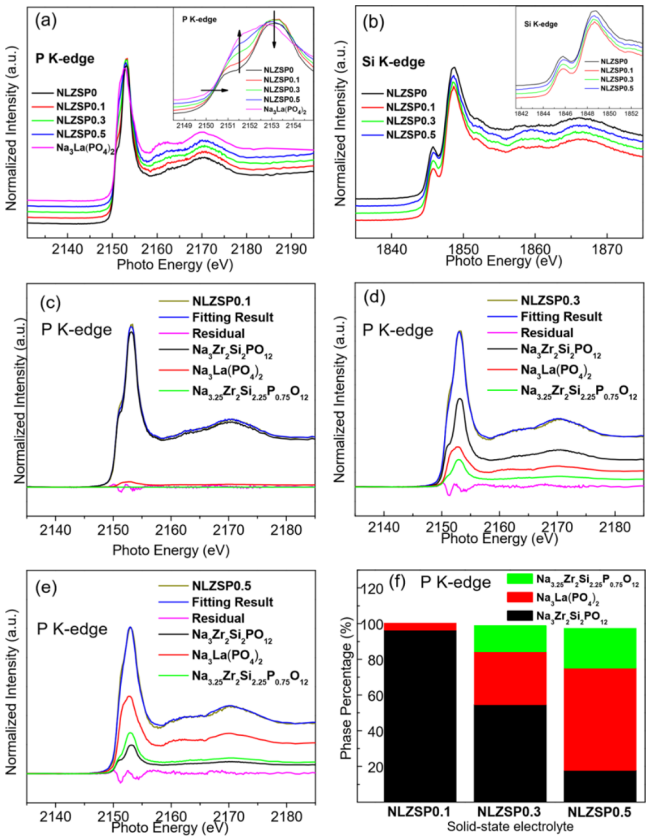

Figure 4. (a) P K-edge and (b) Si K-edge XANES spectra for NLZSP0.1, NLZSP0.3, and NLZSP0.5 SSEs and the reference NLZSP0 SSE and $Na_3La(PO_4)_2$. Corresponding LCF analysis for (c) NLZSP0.1, (d) NLZSP0.3, and (e) NLZSP0.5. (f) Fitted content of three reference samples including NLZSP0, $Na_3La(PO_4)_2$, and $Na_{3.25}Zr_2Si_{2.25}P_{0.75}O_{12}$.

In order to determine the composition and understand the composition evolution of the La-doped NASICON phase and the $Na_3La(PO_4)_2$ impurity phase in the NLZSP*x* SSEs, we conducted linear compound fitting (LCF) analyses on the XANES spectra for NLZSP0.1, NLZSP0.3, and NLZSP0.5 (Figure 4c−f) on Athena. LCF is a model of fitting a linear combination of standard spectra to unknown spectra. Since the EDS results show that the content ratio of Si and P changed from 2:1 to 3:1, we synthesized NASICON SSE with a chemical formula of $Na_{3.25}Zr_2Si_{2.25}P_{0.75}O_{12}$, and then LCF analysis was performed with three reference samples of NLZSP0, $Na_3La(PO_4)_2$, and $Na_{3.25}Zr_2Si_{2.25}P_{0.75}O_{12}$. The LCF results demonstrated good fitting among the three reference materials. Figure 4f summarizes and compares the LCF results of the three NLZSP*x* SSEs. Upon an increasing La doping content, the NLZSP0 content gradually decreased, accompanied by an increase in the $Na_3La(PO_4)_2$ and $Na_{3.25}Zr_2Si_{2.25}P_{0.75}O_{12}$ contents.

Figure 4b shows the Si K-edge XANES spectra of the undoped NLZSP0 and the La-doped NLZSP0.1, NLZSP0.3, and NLZSP0.5 SSEs. The spectral features were unchanged in terms of energy position and shape, indicating that the electronic states and local structure of Si remained relatively undisturbed in the NASICON SSEs with or without La doping (impurity formation). The XANES analyses are consistent with the XRD, SEM, and EDS mapping results. Instead of substituting the Zr^{4+} sites in the NASICON structure, the "doped" La^{3+} ions tend to extract the PO_4^{3-} units from the NASICON phase to form phosphate impurities (e.g., $Na_3La(PO_4)_2$), thus altering the Si/P atomic ratios in the NASICON phase changes but retaining the unchanged Si component.

3.4. SS-NMR. SS-NMR was employed to study the local structures of different nuclei and Na^+ dynamics at different Na sites in the NASICON materials. ^{23}Na MAS NMR spectra (Figure 5a) were recorded at 21.1 T magnetic field for a high resolution. With an increase of La doping content, the broad peak at around −1.76 ppm gradually increased in intensity, suggesting the continuous formation of a new phase with the addition of La. Correlating with the XRD and XANES results, this new phase should be attributed to $Na_3La(PO_4)_2$.

Figure 5b shows the ^{31}P MAS NMR spectra of NLZSP*x* with different La doping contents. A strong peak at around −11 ppm is assigned to the NASICON phase. In the spectrum of NLZSP0, the weak peaks between 0 and 7 ppm are assigned to the impurity phases formed during the synthesis process. With the addition of La, two new peaks at around 3.0 and 1.2 ppm were observed, which are assigned to $Na_3La(PO_4)_2$, whose ^{31}P

https://dx.doi.org/10.1021/acsami.0c21882
ACS Appl. Mater. Interfaces 2021, 13, 13132−13138

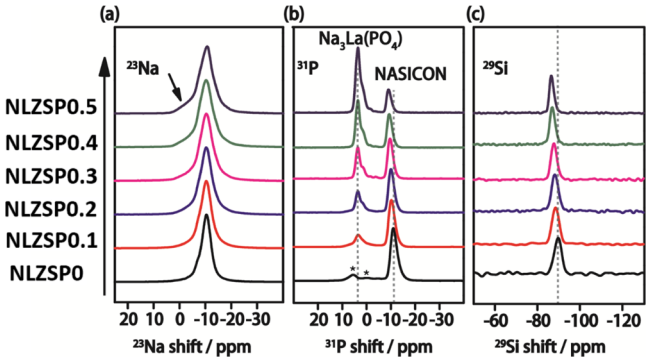

Figure 5. (a) ^{23}Na MAS NMR spectra of NLZSPx (x = 0, 0.1, 0.2, 0.3, 0.4, and 0.5) acquired at 21.1 T. (b) ^{31}P MAS NMR spectra of NLZSPx (x = 0, 0.1, 0.2, 0.3, 0.4, 0.5); peaks marked by * indicate the impurities. (c) ^{29}Si MAS NMR spectra of NLZSPx (x = 0, 0.1, 0.2, 0.3, 0.4, and 0.5).

MAS NMR spectrum is shown in Figure S2. With more La doping, the content of the NASICON phase decreased, but the $Na_3La(PO_4)_2$ content increased. Beyond NLZSP0.3 (i.e., NLZSP0.4 and NLZSP0.5), the $Na_3La(PO_4)_2$ phase eventually became the main component in NLZSPx samples (Figure S3). Furthermore, the ^{23}Na T_1 measurement on pure $Na_3La(PO_4)_2$ was performed to understand its transport property and yielded a T_1 value of 2 s, implying the presence of a very slow ionic motion in $Na_3La(PO_4)_2$ (Figure S4), well in accordance with the impedance results. Therefore, the enhanced ionic conductivity of the La-doped NASICON material was actually not due to the generation of $Na_3La(PO_4)_2$.

When considering the influence of La doping on the NASICON phase, we notice that the chemical shift and content of the NASICON phase varied with the formation of $Na_3La(PO_4)_2$. Figure 5b,c shows that both ^{31}P and ^{29}Si chemical shifts of the NASICON phase shifted to lower field with increasing content of La doping in the NLZSPx materials, suggesting that the electron spin densities decreased around the nuclei. The results demonstrated that Na^+ occupancy increased with La doping, giving rise to the biases of the electron spin density on the oxygen atom toward sodium ions, which is consistent with previous reports[18] deriving the same conclusion for Sc-doping NZSP materials by density functional theory calculations. In addition, the ^{29}Si MAS NMR spectra indicated no evidence for the Si-containing impurity. However, the formation of $Na_3La(PO_4)_2$ upon La doping still changed the proportion of Si to P in the NASICON phase of the NLZSPx SSEs.

Measurements of ^{23}Na T_1 provide an in-depth insight into the ionic motion of Na^+ ions. For NASICON materials, a smaller T_1 value indicates faster movement of the studied nucleus at room temperature.[30] Figure 6 shows the fitting results. All magnetization recovery trajectories could be well described using two relaxation components. The component (blue line) having a larger portion with faster ionic motion was attributed to the NASICON phase, while the other (red line) was assigned to the impurity phase $Na_3La(PO_4)_2$. The results showed that with the increasing of addition amount of La^{3+}, the content of the NASICON phase declined with the increasing content of the impurity phase. This was in accordance with the ^{31}P MAS NMR and XANES results. More importantly, the ^{23}Na T_1 value of the NASICON phase reached the minimum for NLZSP0.3, demonstrating the fastest ionic motion and proving the ionic conductivity results. In the view that NMR is sensitive to the bulk ionic motion, the results verified that La doping had an effect on the ionic motion in the NASICON phase. Beyond NLZSP0.3, the $Na_3La(PO_4)_2$ component dominated in NLZSPx material, causing a decline in ionic conductivity because of the sluggish motion of Na^+ in $Na_3La(PO_4)_2$. Therefore, we conclude that the formation of $Na_3La(PO_4)_2$ caused an atomic ratio of Si to P greater than 2 in the NASICON phase, resulting in a charge unbalance based on our ^{31}P and ^{29}Si MAS NMR spectra. This charge unbalance must be compensated by introducing more Na^+ ions, thus forming a Na-rich NASICON phase with faster ionic motion than that of nonmodified samples.

3.5. Crystal Structure and Ionic Conducting Property of $Na_{3.25}Zr_2Si_{2.25}P_{0.75}O_{12}$. Based on the conclusion that the unbalanced Si/P ratio (more specifically, SiO^{4-} to PO_4^{3-} ratio) had led to a favorable Na-rich NASICON phase in the NLZSPx SSEs, we intentionally synthesized a pure NASICON sample with an offset Si/P ratio, $Na_{3.25}Zr_2Si_{2.25}P_{0.75}O_{12}$. The XRD results in Figure 7a show that NLZSP0 and

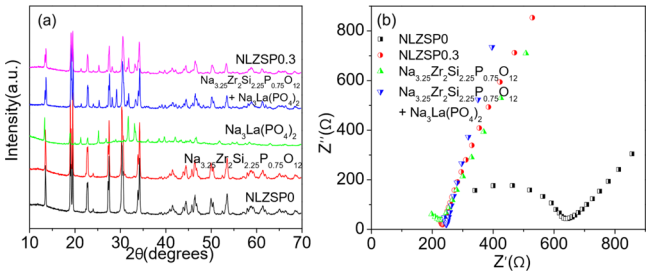

Figure 7. (a) XRD patterns and (b) impedance spectra of the different NLZSP SSEs.

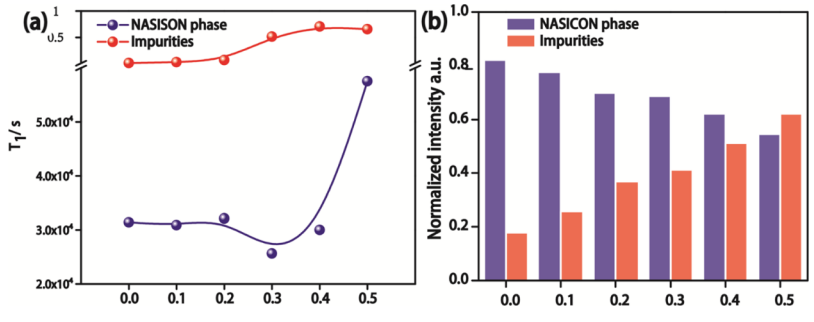

Figure 6. (a) Fitting results of T_1 relaxation time for NLZSPx (x = 0, 0.1, 0.2, 0.3, 0.4, and 0.5). (b) Normalized contents of the NASICON phase and the impurity $Na_3La(PO_4)_2$.

https://dx.doi.org/10.1021/acsami.0c21882
ACS Appl. Mater. Interfaces 2021, 13, 13132−13138

$Na_{3.25}Zr_2Si_{2.25}P_{0.75}O_{12}$ shared the same crystal structure; a mixture of $Na_{3.25}Zr_2Si_{2.25}P_{0.75}O_{12}$ and a small amount of $Na_3La(PO_4)_2$ actually yielded an XRD pattern highly similar to that of the NLZSP0.3 sample. The amount of $Na_3La(PO_4)_2$ impurity added in $Na_{3.25}Zr_2Si_{2.25}P_{0.75}O_{12}$ was comparable to that formed in the NLZSP0.3 sample. Impedance spectra of the pure $Na_{3.25}Zr_2Si_{2.25}P_{0.75}O_{12}$ and the $Na_3La(PO_4)_2$-added $Na_{3.25}Zr_2Si_{2.25}P_{0.75}O_{12}$ exhibited small impedances similar to that of NLZSP0.3 at 25 °C and correspondingly a high ionic conductivity of 1.34×10^{-3} S/cm (Figure 7b). This confirmed that an increased Si/P ratio and enhanced Na^+ occupancy for NASICON SSEs could lead to improved ionic conductivities.

4. CONCLUSIONS

Different amounts of La doping are projected to form a series of La-doped NACISON structures of $Na_{3+x}Zr_{2-x}La_xSi_2PO_{12}$ ($0 \leq x \leq 0.5$), where an x value of 0.3 yields an optimal ionic conductivity of 1.34×10^{-3} S/cm at 25 °C. However, based on the XRD, SS-NMR, and XANES analyses, these "La-doped" NASICON SSEs are found to consist of mainly a Na-rich NASICON phase and a $Na_3La(PO_4)_2$ phase. The resulted $Na_3La(PO_4)_2$ content increased along with the increasing La content, which meanwhile altered the Si/P ratio in the NASICON phase. The ^{31}P and ^{29}Si MAS NMR spectra reveal a Si/P ratio to be greater than 2 in the NASICON phase. The charge unbalance leads to an increase in Na^+ occupancy. The measurements of spin−lattice relaxation time confirm the accelerated Na^+ ionic motions in the Na-rich NASICON phase rather than the sluggish $Na_3La(PO_4)_2$ phase, verifying an optimal x of 0.3. An intentionally synthesized Na-rich $Na_{3.25}Zr_2Si_{2.25}P_{0.75}O_{12}$ with an offset Si/P ratio also achieve a similarly high ionic conductivity in the order of 10^{-3} S/cm at 25 °C. XANES linear combination fitting confirmed the important presence of the Na-rich phase. Despite the efforts of La doping into the NASICON structure for improving the ionic conductivity, direct alteration of Si/P ratio in the NASICON structure can be a promising and efficient strategy for developing advanced NASICON SSEs without ionic sluggish impurities. This provides new opportunities for high-performance SSEs for solid-state sodium batteries.

■ ASSOCIATED CONTENT

Supporting Information

The Supporting Information is available free of charge at https://pubs.acs.org/doi/10.1021/acsami.0c21882.

SEM, EDS analysis, and quantitative results of NLZSP0 and NLZSP0.3; 31P MAS NMR spectra; quantitative results of 31P MAS NMR spectra; and fitting results of T1 relaxation time of Na3La(PO4)2 (PDF)

■ AUTHOR INFORMATION

Corresponding Authors

Tsun-Kong Sham − *Department of Chemistry, University of Western Ontario, London, Ontario N6A 5B7, Canada;* orcid.org/0000-0003-1928-6697; Email: tsham@uwo.ca

Yong Yang − *State Key Laboratory for Physical Chemistry of Solid Surfaces, Collaborative Innovation Center of Chemistry for Energy Materials and Department of Chemistry, College of Chemistry and Chemical Engineering, Xiamen University, Xiamen 361005, China;* orcid.org/0000-0003-1145-8992; Email: yyang@xmu.edu.cn

Xuhui Sun − *Soochow University−Western University Center for Synchrotron Radiation Research, Institute of Functional Nano and Soft Materials (FUNSOM), Jiangsu Key Laboratory for Carbon-Based Functional Materials & Devices, Soochow University, Suzhou 215123, China;* orcid.org/0000-0003-0002-1146; Email: xhsun@suda.edu.cn

Xueliang Sun − *Department of Mechanical and Materials Engineering, University of Western Ontario, London, Ontario N6A 5B9, Canada;* orcid.org/0000-0003-0374-1245; Email: xsun@eng.uwo.ca

Authors

Fei Sun − *Soochow University−Western University Center for Synchrotron Radiation Research, Institute of Functional Nano and Soft Materials (FUNSOM), Jiangsu Key Laboratory for Carbon-Based Functional Materials & Devices, Soochow University, Suzhou 215123, China; Department of Mechanical and Materials Engineering, University of Western Ontario, London, Ontario N6A 5B9, Canada*

Yuxuan Xiang − *State Key Laboratory for Physical Chemistry of Solid Surfaces, Collaborative Innovation Center of Chemistry for Energy Materials and Department of Chemistry, College of Chemistry and Chemical Engineering, Xiamen University, Xiamen 361005, China*

Qian Sun − *Department of Mechanical and Materials Engineering, University of Western Ontario, London, Ontario N6A 5B9, Canada*

Guiming Zhong − *Xiamen Institute of Rare Earth Materials, Chinese Academy of Sciences, Xiamen 361021, China;* orcid.org/0000-0003-2313-4741

Mohammad Norouzi Banis − *Department of Mechanical and Materials Engineering, University of Western Ontario, London, Ontario N6A 5B9, Canada;* orcid.org/0000-0002-6144-6837

Weihan Li − *Department of Mechanical and Materials Engineering, University of Western Ontario, London, Ontario N6A 5B9, Canada*

Yulong Liu − *Department of Mechanical and Materials Engineering, University of Western Ontario, London, Ontario N6A 5B9, Canada*

Jing Luo − *Department of Mechanical and Materials Engineering, University of Western Ontario, London, Ontario N6A 5B9, Canada*

Ruying Li − *Department of Mechanical and Materials Engineering, University of Western Ontario, London, Ontario N6A 5B9, Canada*

Riqiang Fu − *National High Magnetic Field Laboratory, Tallahassee, Florida 32310, United States;* orcid.org/0000-0003-0075-0410

Complete contact information is available at: https://pubs.acs.org/10.1021/acsami.0c21882

Author Contributions

¶F.S. and Y.X. contributed equally to this work.

Notes

The authors declare no competing financial interest.

■ ACKNOWLEDGMENTS

The work was supported by the Natural Science Foundation of China (NSFC) (grant U1432249), the National Key R&D

Program of China (grant 2017YFA0205002), and the Priority Academic Program Development (PAPD) of Jiangsu Higher Education Institutions. This is also a project supported by the Jiangsu Key Laboratory for Carbon-Based Functional Materials and Devices and the Collaborative Innovation Center of Suzhou Nano Science & Technology. This work was also supported by the Natural Science and Engineering Research Council of Canada (NSERC), the Canada Research Chair Program (CRC), the Canada Foundation for Innovation (CFI), and the University of Western Ontario (UWO). R.F. acknowledges the support from the National High Magnetic Field Laboratory which is supported by NSF Cooperative Agreement DMR-1644779 and the State of Florida.

REFERENCES

(1) Kundu, D.; Talaie, E.; Duffort, V.; Nazar, L. F. The emerging chemistry of sodium ion batteries for electrochemical energy storage. *Angew. Chem., Int. Ed.* **2015**, *54*, 3431−3448.

(2) Hueso, K. B.; Armand, M.; Rojo, T. High temperature sodium batteries: status, challenges and future trends. *Energy Environ. Sci.* **2013**, *6*, 734−749.

(3) Kim, S.-W.; Seo, D.-H.; Ma, X.; Ceder, G.; Kang, K. Electrode Materials for Rechargeable Sodium-Ion Batteries: Potential Alternatives to Current Lithium-Ion Batteries. *Adv. Energy Mater.* **2012**, *2*, 710−721.

(4) Palomares, V.; Serras, P.; Villaluenga, I.; Hueso, K. B.; Carretero-González, J.; Rojo, T. Na-ion batteries, recent advances and present challenges to become low cost energy storage systems. *Energy Environ. Sci.* **2012**, *5*, 5884−5901.

(5) Fang, Y.; Xiao, L.; Chen, Z.; Ai, X.; Cao, Y.; Yang, H. Recent Advances in Sodium-Ion Battery Materials. *Electrochem. Energy Rev.* **2018**, *1*, 294−323.

(6) Wang, T.; Su, D.; Shanmukaraj, D.; Rojo, T.; Armand, M.; Wang, G. Electrode Materials for Sodium-Ion Batteries: Considerations on Crystal Structures and Sodium Storage Mechanisms. *Electrochem. Energy Rev.* **2018**, *1*, 200−237.

(7) Goodenough, J. B. Rechargeable batteries: Challenges old and new. *J. Solid State Electrochem.* **2012**, *16*, 2019−2029.

(8) Zhang, Z.; Zhang, Q.; Shi, J.; Chu, Y. S.; Yu, X.; Xu, K.; Ge, M.; Yan, H.; Li, W.; Gu, L.; Hu, Y.-S.; Li, H.; Yang, X.-Q.; Chen, L.; Huang, X. A Self-Forming Composite Electrolyte for Solid-State Sodium Battery with Ultralong Cycle Life. *Adv. Energy Mater.* **2016**, *7*, 1601196.

(9) Khakpour, Z. Influence of M: Ce^{4+}, Gd^{3+} and Yb^{3+} substituted $Na_{3+x}Zr_{2-x}M_xSi_2PO_{12}$ solid NASICON electrolytes on sintering, microstructure and conductivity. *Electrochim. Acta* **2016**, *196*, 337−347.

(10) Ma, Q.; Guin, M.; Naqash, S.; Tsai, C.-L.; Tietz, F.; Guillon, O. Scandium-Substituted Na3Zr2(SiO4)2(PO4) Prepared by a Solution-Assisted Solid-State Reaction Method as Sodium-Ion Conductors. *Chem. Mater.* **2016**, *28*, 4821−4828.

(11) Xie, B.; Jiang, D.; Wu, J.; Feng, T.; Xia, J.; Nian, H. Effect of substituting Ce for Zr on the electrical properties of NASICON materials. *J. Phys. Chem. Solids* **2016**, *88*, 104−108.

(12) Jolley, A. G.; Cohn, G.; Hitz, G. T.; Wachsman, E. D. Improving the ionic conductivity of NASICON through aliovalent cation substitution of $Na_3Zr_2Si_2PO_{12}$. *Ionics* **2015**, *21*, 3031−3038.

(13) Jolley, A. G.; Taylor, D. D.; Schreiber, N. J.; Wachsman, E. D. Structural Investigation of Monoclinic-Rhombohedral Phase Transition in $Na_3Zr_2Si_2PO_{12}$ and Doped NASICON. *J. Am. Ceram. Soc.* **2015**, *98*, 2902−2907.

(14) Bell, N. S.; Edney, C.; Wheeler, J. S.; Ingersoll, D.; Spoerke, E. D. The Influences of Excess Sodium on Low-Temperature NASICON Synthesis. *J. Am. Ceram. Soc.* **2014**, *97*, 3744−3748.

(15) Fuentes, R. O.; Figueiredo, F. M.; Soares, M. R.; Marques, F. M. B. Submicrometric NASICON ceramics with improved electrical conductivity obtained from mechanically activated precursors. *J. Am. Chem. Soc.* **2005**, *25*, 455−462.

(16) Fuentes, R.; Figueiredo, F. M.; Marques, F. M. B.; Ifranco, J. Influence of microstructure on the electrical properties of NASICON materials. *Solid State Ionics* **2001**, *140*, 173−179.

(17) Hong, H. Y.-P. Crystal strucrures and crystal chemistry in the system $Na_{1+x}Zr_2Si_xP_{3-x}O_{12}$. *Mater. Res. Bull.* **1976**, *11*, 173−182.

(18) Deng, Y.; Eames, C.; Nguyen, L. H. B.; Pecher, O.; Griffith, K. J.; Courty, M.; Fleutot, B.; Chotard, J.-N.; Grey, C. P.; Islam, M. S.; Masquelier, C. Crystal Structures, Local Atomic Environments, and Ion Diffusion Mechanisms of Scandium-Substituted Sodium Superionic Conductor (NASICON) Solid Electrolytes. *Chem. Mater.* **2018**, *30*, 2618−2630.

(19) Ruan, Y.; Song, S.; Liu, J.; Liu, P.; Cheng, B.; Song, X.; Battaglia, V. Improved structural stability and ionic conductivity of Na3Zr2Si2PO12 solid electrolyte by rare earth metal substitutions. *Ceram. Int.* **2017**, *43*, 7810−7815.

(20) Park, H.; Jung, K.; Nezafati, M.; Kim, C.-S.; Kang, B. Sodium Ion Diffusion in Nasicon ($Na_3Zr_2Si_2PO_{12}$) Solid Electrolytes: Effects of Excess Sodium. *ACS Appl. Mater. Interfaces* **2016**, *8*, 27814−27824.

(21) Lee, J.-S.; Chang, C.-M.; Lee, Y. I.; Lee, J.-H.; Hong, S.-H. Spark Plasma Sintering (SPS) of NASICON Ceramics. *J. Am. Ceram. Soc.* **2004**, *87*, 305−307.

(22) Noi, K.; Suzuki, K.; Tanibata, N.; Hayashi, A.; Tatsumisago, M. Liquid-phase sintering of highly Na^+ ion conducting $Na_3Zr_2Si_2PO_{12}$ ceramics using Na_3BO_3 addtive. *J. Am. Ceram. Soc.* **2017**, *101*, 1255−1265.

(23) Shimizu, Y.; Ushijima, T. Sol-gel processing of NASICON thin film using aqueous complex precursor. *Solid State Ionics* **2000**, *132*, 143−148.

(24) Guin, M.; Tietz, F.; Guillon, O. New promising NASICON material as solid electrolyte for sodium-ion batteries: Correlation between composition, crystal structure and ionic conductivity of Na3+xSc2SixP3−xO12. *Solid State Ionics* **2016**, *293*, 18−26.

(25) Kar, G.; Schoenau, J.; Hilger, D.; Peak, D. Direct chemical speciation of soil phosphorus in a Saskatchewan Chernozem after long- and short-term manure amendments. *Can. J. Soil Sci.* **2017**, *97*, 626−636.

(26) Yoon, W.-S.; Chung, K. Y.; McBreen, J.; Zaghib, K.; Yang, X.-Q. Electronic Structure of the Electrochemically Delithiated $Li_{1-x}FePO_4$ Electrodes Investigated by P K-edge X-Ray Absorption Spectroscopy. *Electrochem. Solid-State Lett.* **2006**, *9*, A415−A417.

(27) Franke, R.; Hormes, J. The P K-near edge absorption spectra of phosphates. *Phys. B* **1995**, *216*, 85−95.

(28) Okude, N.; Nagoshi, M.; Noro, H.; Baba, Y.; Yamamoto, H.; Sasaki, T. A. P and S K-edge XANES of transition-metal phosphates and sulfates. *J. Electron Spectrosc. Relat. Phenom.* **1999**, *101*−*103*, 607−610.

(29) Kruse, J.; Leinweber, P. Phosphorus in sequentially extracted fen peat soils: A K-edge X-ray absorption near-edge structure (XANES) spectroscopy study. *J. Plant Nutr. Soil Sci.* **2008**, *171*, 613−620.

(30) Wilkening, M.; Heitjans, P. From Micro to Macro: Access to Long-Range Li+ Diffusion Parameters in Solid via Microscopic 6,7 Li Spin-Alighnment Echo NMR. *ChemPhysChem* **2012**, *13*, 53−65.

https://dx.doi.org/10.1021/acsami.0c21882
ACS Appl. Mater. Interfaces 2021, 13, 13132−13138